Resolving Ultrafast Photoinitiated Dynamics of the Hachimoji 5-aza-7-deazaguanine Nucleobase

Krul, Sarah E.; Costa, Gustavo J.; Hoehn, Sean J.; Valverde, Danillo; Oliveira, Leonardo M.F.; Borin, Antonio Carlos; Crespo-Hernández, Carlos E.

Published in:
Photochemistry and Photobiology

DOI:
10.1111/php.13688

Publication date:
2022

Document Version
Publisher's PDF, also known as Version of record

Photochemistry and Photobiology, 20**, **: *–*

Special Issue Research Article

Resolving Ultrafast Photoinitiated Dynamics of the Hachimoji 5-aza-7-deazaguanine Nucleobase: Impact of Synthetically Expanding the Genetic Alphabet[1]

Sarah E. Krul[1], Gustavo J. Costa[2], Sean J. Hoehn[1], Danillo Valverde[3], Leonardo M. F. Oliveira[2], Antonio Carlos Borin[2]* and Carlos E. Crespo-Hernández[1]*

[1]Department of Chemistry, Case Western Reserve University, Cleveland, OH
[2]Department of Fundamental Chemistry, Institute of Chemistry, University of São Paulo, São Paulo, Brazil
[3]Unité de Chimie Physique Theorique et Structurale, Namur Institute of Structured Matter, Université de Namur, Namur, Belgium

Received 26 June 2022, accepted 5 August 2022, DOI: 10.1111/php.13688

ABSTRACT

The guanine derivative, 5-aza-7-deazaguanine (^{5N7C}G) has recently been proposed as one of four unnatural bases, termed Hachimoji (8-letter) to expand the genetic code. We apply steady-state and time-resolved spectroscopy to investigate its electronic relaxation mechanism and probe the effect of atom substitution on the relaxation mechanism in polar protic and polar aprotic solvents. Mapping of the excited state potential energy surfaces is performed, from which the critical points are optimized by using the state-of-art extended multi-state complete active space second-order perturbation theory. It is demonstrated that excitation to the lowest energy $^1\pi\pi^*$ state of ^{5N7C}G results in complex dynamics leading to *ca.* 10- to 30-fold slower relaxation (depending on solvent) compared with guanine. A significant conformational change occurs at the S_1 minimum, resulting in a 10-fold greater fluorescence quantum yield compared with guanine. The fluorescence quantum yield and S_1 decay lifetime increase going from water to acetonitrile to propanol. The solvent-dependent results are supported by the quantum chemical calculations showing an increase in the energy barrier between the S_1 minimum and the S_1/S_0 conical intersection going from water to propanol. The longer lifetimes might make ^{5N7C}G more photochemically active to adjacent nucleobases than guanine or other nucleobases within DNA.

INTRODUCTION

The canonical nucleobases, the basic building blocks of DNA and RNA, are often considered the molecular basis of life due to their involvement in different processes such as development, growth and replication (1,2). Atomic substitutions or small modifications of the five canonical nucleobases have been of great interest over the years, where derivatives have been shown to (1) assist in regulation and transcription processes (2–5), improve medicinal therapeutics stability and function (3,6–8), shed light on the evolutionary advancements that led to the settlement upon the five canonical bases (9–15). In addition, the search for artificial nucleobases with the ability to form Watson–Crick (WC) hydrogen bonds (HBs) and be transcribed *in vivo*, provides the ability to increase the genetic alphabet and information storage (16–19). Expansion of the genetic code with synthetic bases, termed xenobiology, has been examined during recent decades, where the most critical criterion evaluated by scientists has been size and WC base pairing (19–22). These criteria are equally important in maintaining the standard size of DNA and RNA tertiary structures and their stability. Modifications to the purine core chromophore can be introduced by substituting key chemical centers or functionalizing essential positions. The most interestingly modified nucleobases are those exhibiting new properties while retaining some of the most relevant canonical nucleic acid features. Scientists seek chemical modifications that lead to faithful isomorphic and isofunctional surrogates of their natural counterparts but with improved features (23). For example, many isomorphic compounds of guanine have been studied (24–29), some with interesting fluorescence properties not observed in the canonical form (30,31). A critical criterion that often goes overlooked is the photostability of artificial bases on exposure to ultraviolet (UV) and visible radiation and the possible unintended consequences that can arise following exposure to electromagnetic radiation (21,32,33). Although it is well known that the canonical bases dissipate most of the excess energy ultrafast through internal conversion, there is still a small percentage of DNA and RNA that can undergo photo-assisted damage (15,34,35). This damage can lead to mutations and

*Corresponding authors email: ancborin@iq.usp.br (Antonio Carlos Borin), carlos.crespo@case.edu (Carlos Crespo-Hernández)
†Sarah E. Krul, Gustavo J. Costa and Sean J. Hoehn contributed equally to this work.
[1]This article is part of a Special Issue celebrating the 50th Anniversary of the American Society for Photobiology.

lesions. However, mechanisms including but not limited to base excision repair and nucleotide excision repair, are natural tools to prevent and repair the damage, upholding the integrity and viability of DNA (36–42). Therefore, when aiming to expand the genetic code, it is of vital importance to determine if synthetic bases, and their ultimate incorporation in the genetic code, will adversely affect its integrity under light exposure.

The guanine derivative, 5-aza-7-deazaguanine (^{5N7C}G, also known as, P) (22,43), in which the nitrogen at position seven and the carbon at position five of guanine are exchanged, has recently been proposed by Benner *et al*. as one of four unnatural bases, termed Hachimoji (22,43). Similar atomic substitution has previously been shown to dramatically influence the photochemical and photophysical properties of a DNA or RNA molecule (21,44–49). Importantly, the WC base edge is maintained and has been shown to HB with its Hachimoji conjugate base 6-amino-5-nitro-2-pyrimidinone (Z) (18,22,43,50).

To the best of our knowledge, there are no reported fluorescence quantum yield, time-resolved absorption spectroscopy experiments or even theoretical descriptions of the photochemistry and photophysical properties of the ^{5N7C}G molecule. In the present study, we apply steady-state and time-resolved spectroscopy to investigate the electronic relaxation mechanism of ^{5N7C}G and probe the effect of atom substitution on the relaxation mechanism in polar protic and polar aprotic solvents. The experimental results are complemented by static mapping of the potential energy surfaces, from which the critical points are optimized by using the state-of-art extended multi-state complete active space second-order perturbation theory (XMS-CASPT2) (51,52). Solvent effects are considered computationally using the polarized continuum model (PCM) and the Average Solvent Electrostatic Configuration and Free Energy Gradient (ASEC-FEG) protocol.

MATERIALS AND METHODS

5-Aza-7-deazaguanine (>95% purity) was purchased from Toronto Research Chemicals. Acetonitrile (ACN, 99.8% purity) and 1-propanol (PrOH, 99% purity) were both purchased from Fisher Scientific. All chemicals were used as received. The ultrapure water (Milli-pore) was freshly obtained and mixed with ACN' or PrOH the day of each laser irradiation experiment. Likewise, phosphate buffer solutions with a total phosphate concentration of 16 mM from monosodium and disodium phosphate salts dissociated in ultrapure water were freshly prepared the day of each experiment. The pH of the solution was adjusted using 0.1 M solutions of NaOH to the desired pH of 6.8 (± 0.1 pH units).

Steady-state absorption and emission. Steady-state absorption spectra were recorded using a Jasco V-730 spectrophotometer. Emission and excitation spectra were recorded using a Cary Eclipse spectrometer, with a PMT voltage of 600 V, 5 nm slit widths, and a scan rate of 20 nm min^{-1}. The fluorescence spectra were corrected for Raman emission of the solvent and for the lamp intensity at each respective wavelength. Due to insolubility in neat organic solvent, the solutions were prepared in a mixture of 10% ultrapure water and 90% organic solvent. The solutions for fluorescence spectra in each respective solvent mixture were prepared with matching optical densities of 0.13 at excitation wavelength of 267 nm. The fluorescence quantum yield was calculated following Eq. (1):

$$\Phi = \Phi_R \bullet \frac{I}{I_R} \bullet \frac{\mathrm{OD}_R}{\mathrm{OD}} \bullet \frac{n^2}{n_R{}^2} \quad (1)$$

where Φ represents the fluorescence quantum yield, I is the integrated area under the emission spectrum, OD is the optical density at excitation wavelength, and n is the refractive index of the respective solvent. The subscript R denotes the fluorescence standard, L-tryptophan, of known quantum yield (53,54).

fs-Broadband transient absorption spectroscopy. The experimental setup and data analysis used for femtosecond broadband transient absorption spectroscopy (TAS) has been described in detail previously (55–57). Briefly, a Ti:sapphire oscillator (Vitesse, Coherent) was used to seed a regenerative amplifier (Libra-HE, Coherent) to produce 100 fs pulses, centered at 800 nm, with a 1 kHz repetition rate. An optical rail kit (FKE series, EKSMA optics) was used to generate the excitation pulse at 267 nm as previously described (58). A 2 mm translating $CaFl_2$ crystal was used to generate the while light continuum from 320 to 700 nm. Experimental pump-probe conditions were adjusted to eliminate two-photon conditions as previously described in great detail (24).

The samples were freshly prepared the day of the laser experiment with absorbances of 0.48 in ACN', 0.62 in phosphate buffer, and 0.39 PrOH', respectively, at the excitation wavelength and collected back-to-back. The homogeneity of the solutions in a 2 mm path length fused silica cell was maintained by continuous stirring with a Teflon-coated magnetic stirbar. The solution inside the cell was frequently refreshed during data acquisition such that the absorption maximum of the samples at excitation wavelength did not decrease by more than 5%, as judged by steady-state absorption. This was done to minimize the potential contamination of the transient signals by the formation of photoproducts absorbing at the excitation wavelength.

Data collection made use of a home-made LabView program, following which global and target analysis were performed using the Glotaran graphical user interface to the R-package TIMP software (59). The complete multidimensional data in each solvent was globally fit using a three-component sequential kinetic model, convoluted with a Gaussian instrument response function of 250 ± 50 fs (FWHM). The evolution-associated difference spectra (EADS) were extracted from the global and target analyses (60).

Computational details. The ^{5N7C}G photochemical relaxation pathways were investigated with the photochemical reaction path approach (61). Stationary points were optimized by using the XMS-CASPT2 (51,52), using Dunning's double-ζ basis sets (cc-pVDZ) (62), without ionization potential-electron affinity (IPEA) shift correction (63), and with an imaginary level shift (64) of 0.20 a.u. to deal with intruder states.

Minimum energy crossing points (MECPs) were optimized as the lowest energy point obtained with the restricted Lagrange multipliers technique, imposing the constraint of degeneracy between the two states considered (65), which corresponds to an energy difference between the two states smaller than about 0.0027 eV (0.0628 kcal·mol^{-1}); off-diagonal elements at the MECP structures were always smaller than 0.0001 Hartree. The nonadiabatic coupling elements are not computed; the MECPs involving singlet electronic states are called singlet-singlet minimum energy crossing points (SSCPs).

Starting from the Franck-Condon region, the main deactivation pathway followed by the bright state in vacuum was explored by using the minimum energy path (MEP) approach, computed as the steepest descent path using mass-weighted coordinates (65) at the XMS-CASPT2/cc-pVDZ level of theory. Unfortunately, due to high time consuming and computational costs, MEP calculations at the XMS-CASPT2 level of theory cannot always be used. To circumvent this technical limitation, we used linear interpolation in internal coordinates (LIIC) defined *via* the Z-matrix technique to explore other photochemical relaxation pathways connecting different regions along the potential energy hypersurfaces in vacuum or solution. It is worth keeping in mind that energy barriers observed along the LIIC pathway correspond to an upper limit for the real barriers, but still, the LIIC pathways provide a reliable description of the real paths.

Solvent effects were considered with two dissimilar approaches. One of them is based on the PCM model (66), for which the most relevant parameter is the solvent dielectric constant (ε). Nevertheless, as 1-propanol dielectric constant (PrOH, ε = 20.52) (67) is not implemented in OpenMolcas (68,69), thus for the PCM calculations we used the acetone parameter (ε = 20.70), instead of the 1-propanol due to similar dielectric constant; the same strategy was used in a recent publication (70) without compromising the quality of the results.

The other approach is the ASEC-FEG (71,72) protocol (Average Solvent Electrostatic Configuration and Free Energy Gradient), an iterative procedure based on classical simulations and quantum mechanical (QM) calculations to search for the nearest critical point structure on the free energy surface of a solute in solution. Among its advantages, we highlight those nonhomogeneous solvent effects are considered, and the solute–solvent interactions are included in the QM calculation by means of an average electrostatic embedding (ASEC) (71–73).

The number of explicit water molecules considered quantum mechanically in the simulation of the absorption and emission spectra was determined based on the average number of solute-solvent HBs. First, the solvation shells around the solute were detailed by using the minimum-distance pairwise and radial distribution functions (74). Afterward, the selection of HB is properly obtained by using distance, angular and energetic criteria. Further details about the computational procedures can be found in the Supporting Information.

RESULTS

Experimental results

Steady state. Figure 1 shows the molar absorption spectra of ^{5N7C}G in a mixture of 90% acetonitrile (ACN) or 90% 1-propanol (PrOH) with 10% ultrapure water at pH of 5.5 and phosphate buffer pH 6.8. These solvent mixtures were required due to the low solubility of ^{5N7C}G in neat ACN and PrOH. For simplicity, throughout the remainder of the study, the 90% ACN or PrOH with 10% ultrapure water mixtures will be referred to as ACN' and PrOH', respectively. Importantly, in each of these solvent mixtures, the predominant species of 5-aza-7-deazagunanine is the N_9-H tautomer, as reported by Eberlein *et al*. (75) The atomic labels used for the ^{5N7C}G molecule can be seen in the inset of Fig. 1. The absorption spectra have two prominent bands irrespective of solvent, where the lowest energy absorption band has a maximum at 255 nm (4.86 eV), and the higher energy absorption band has a maximum at 209 nm (5.93 eV). Following excitation at 267 nm (4.64 eV), a broad emission spectrum is observed with a maximum at 390 nm (3.18 eV) in the three solvents (Figure S1). No major solvatochromic shifts are observed for the absorption or the emission spectra upon changing solvent. Steady-state properties including molar absorptivity coefficients and fluorescence quantum yields are reported in Table 1. The excitation spectra taken at an emission wavelength of 390 nm (3.18 eV) are in good agreement with the absorption spectra of ^{5N7C}G, demonstrating that the fluorescence emission originates from the ^{5N7C}G nucleobase.

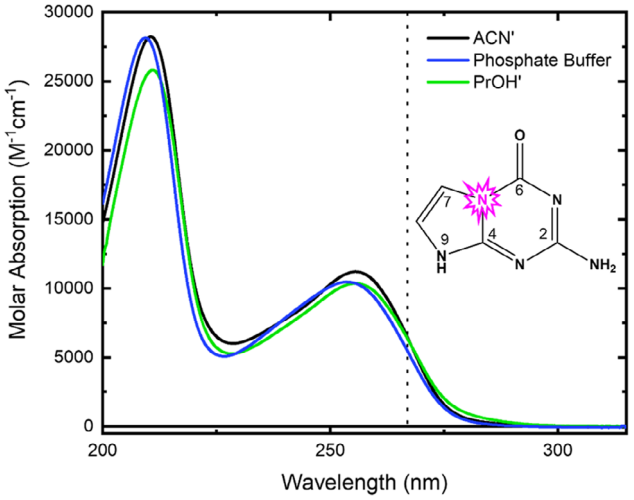

Figure 1. Molar absorption spectra for 5-aza-7-deazaguanine (^{5N7C}G) in a mixture of 90% ACN with 10% ultrapure water (black), 100% phosphate buffer (blue) and 90% PrOH (green) with 10% ultrapure water. The dotted line represents the excitation wavelength used in the time resolved experiments. ^{5N7C}G chemical structure is shown in the inset along with standard purine atomic numbering.

Broadband transient absorption spectroscopy. Femtosecond TAS was used to investigate the excited state dynamics of ^{5N7C}G following UV excitation at 267 nm. The transient absorption spectra of ^{5N7C}G in phosphate buffer (left), ACN' (middle) and PrOH' (right) are shown in Fig. 2. In phosphate buffer solution at pH 6.8, a transient species with apparent maxima at *ca*. 320 nm and 525 nm are observed before maximal pump-probe overlap, as shown in Fig. 2(a). This species continues to positively grow in amplitude, while the band maximum in the visible region blue shifts to 500 nm as the pump and probe beams maximally overlap in time designated herein as time zero. Between 0 and *ca*. 0.40 ps, the transient species in the UV region decreases in intensity, while the transient species in the visible region continues to blue shift and gain intensity (Fig. 2c). An apparent isosbestic point is observed at *ca*. 405 nm. Between a delay time of *ca*. 0.40 and 56 ps, the transient species fully decays back to zero at all probe wavelengths, and no longer-lived species are observed after *ca*. 60 ps.

In ACN', a broad nearly featureless transient species grows in during the cross-correlation of the pump and probe beams (Fig. 2e). Between a delay time of −0.19 and 0.17 ps, a rise in amplitude occurs at *ca*. 330 and 500 nm, while a simultaneous decrease in intensity occurs at the far end of the probing regime near 650 nm. As shown in Fig. 2(g), a slight rise is observed for the transient species absorbing at *ca*. 330 nm, along within approximately the next 0.3 ps with a slight rise and blue shift for the species absorbing maximally at *ca*. 500 nm. A blue shift is then observed in the transient species with a maximum at *ca*. 330 nm, and a simultaneous decrease and red shift in absorbance occurs for the absorption band at 500 nm (Fig. 2h). Lastly, from *ca*. 2 ps to 192 ps, a uniform decay is observed, and no longer-lived species are detected after *ca*. 190 ps.

In PrOH', a broad absorbing transient species is observed within the cross-correlation of the pump and probe beams with maxima at *ca*. 330 and 470 nm (Fig. 2j). As shown in Fig. 2(k), after the initial population grows in, a decrease in the UV band is observed along with a red shift in the visible band to 500 nm. Importantly, a depression between the two transient absorption band maxima is observed, which is in good agreement with the emission maximum obtained through steady-state fluorescence. Between a delay time of 0.62 and 1.34 ps, the amplitude of the deep between the two maxima grows in negatively with a slight red shift, as the visible band at *ca*. 505 nm begins to decay. The UV band remains unchanged during this time change. The transient species are shown to fully decay within approximately 450 ps, suggesting no longer-lived species beyond 450 ps are involved in the relaxation pathway at least within the sensitivity of the spectrometer used in this study.

The transient absorption data were subjected to global and target analyses to obtain lifetimes for key steps in the electronic relaxation mechanism in the three different solvents. A three-component sequential model was used to fit the data satisfactorily. Representative kinetic decay traces are shown in Fig. 3(a–c), and EADS are shown in Fig. 3(d–f). The global lifetimes are presented in Table 2.

Theoretical Results

Excited states in the Franck-Condon region. The ground state geometry was optimized at the XMS(4)-CASPT2 (13, 18)/cc-pVDZ level of theory (51,52,76), with an active space including

Table 1. Photophysical properties of 5-aza-7-deazaguanine (^{5N7C}G). Energies in eV are reported in brackets.

	λ_{abs} (nm)	ϵ_{255} ($m^{-1}cm^{-1}$)	λ_{em} (nm)	ϕ_{FL} (± 0.2) $\times 10^{-3}$	$E_{0,0}$ (eV)
Phosphate buffer	255 [4.86]	10 355 ± 25	390 [3.18]	0.4	4.4
ACN'	255 [4.86]	11 199 ± 52	390 [3.18]	1.1	4.3
PrOH'	255 [4.86]	10 357 ± 85	390 [3.18]	1.8	4.2

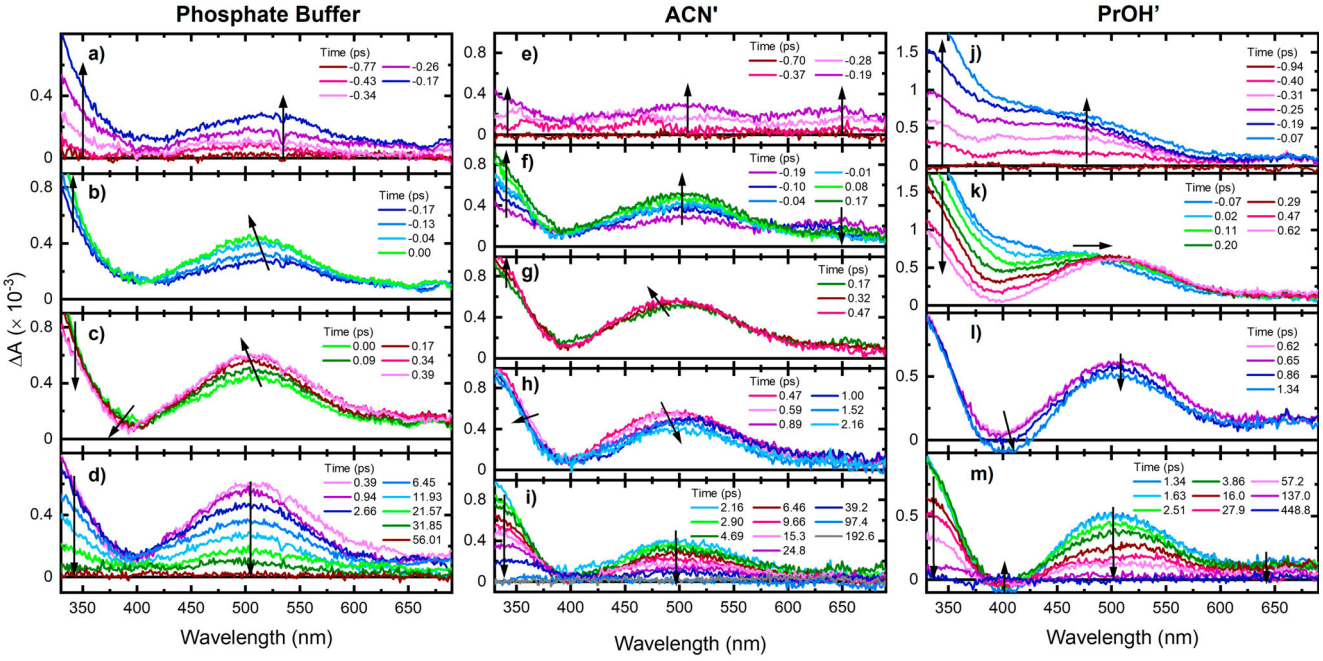

Figure 2. Transient absorption spectra of 5-aza-7-deazaguanine (^{5N7C}G) in 100% phosphate buffer (left), a mixture of 90% ACN with 10% ultrapure water (middle), and 90% PrOH (right) with 10% ultrapure water following excitation at 267 nm.

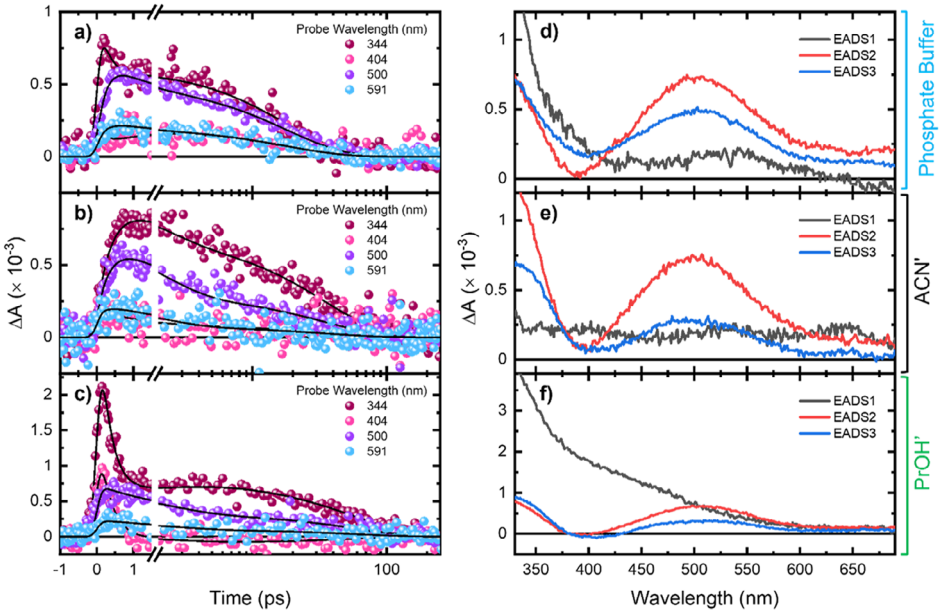

Figure 3. Representative kinetic decay traces (left) of 5-aza-7-deazaguanine in phosphate buffer (a), ACN' (b) and PrOH' (c) globally fit with a three-component sequential model. Note, that the abscissa is linear before 1.5 ps and logarithmic afterward, separated by a break. Evolution-associated difference spectra (EADS) extracted from global and target analysis for 5-aza-7-deazaguanine in phosphate buffer (d), ACN' (e) and PrOH' (f) following excitation at 267 nm.

Table 2. Global lifetimes (in ps) of 5-aza-7-deazaguanine following excitation at 267 nm in phosphate buffer, ACN' and PrOH'. All errors are reported as twice the standard deviation.

Lifetime	Phosphate buffer	ACN'	PrOH'
τ_1	0.3 ± 0.1	0.3 ± 0.1	0.3 ± 0.2
τ_2	0.8 ± 0.2	1.3 ± 0.3	1.7 ± 0.4
τ_3	18.1 ± 0.2	36.9 ± 0.9	57.7 ± 5.1

11 π, π* orbitals plus the three lone pair (n) orbitals and averaging over the lowest-lying four singlet electronic states (see Figure S2 for the molecular orbitals and labeling system). As can be seen in Table S1, irrespective of the number of states averaged and the active space, the ordering of the three lowest-lying singlet electronic states in vacuum is the same, that is, a $^1(\pi_7\pi_1^*)$ followed by two $^1(n\pi_1^*)$ states. The optimized geometry is planar, but for the hydrogen atoms of the amino group, which are out of the molecular plane. The vertical excitation energies calculated in vacuum, water and 1-propanol (n-PrOH) for the first four excited singlet states are shown in Table 3, where solvation was implemented comparing both the PCM (66) and the ASEC-FEG protocol (71,72). The latter solvation model was chosen to better model solvation effects, in which the solvent is treated with molecular mechanics (MM) and the chromophore is treated with quantum mechanics (QM). The superimposed configuration of the MM solvent and QM chromophore goes through an iterative process, where the average electrostatic and van der Waals interactions between the solvent and molecule are obtained (77). Importantly, as shown in Table 3, the ordering of the excited states is sensitive to the solvation model used, where with ASEC-FEG the S_2 excited state becomes ππ* character in both water and n-PrOH compared with nπ* character in vacuum and PCM. The simulated absorption spectra (Fig. 4 and Figure S3), obtained by the convolution of 100 statistically uncorrelated configurations using the ASEC-FEG approach, agree well with experimentally obtained results, where no solvatochromic shift is observed with change in solvent identity. A similar good agreement is observed between the experimental emission spectra and simulated emission spectra for ^{5N7C}G solvated by nine explicitly water molecules at the XMS(7)-CASPT2 (14, 20)/cc-pVDZ/(9•H_2O) level of theory (Figure S4). The effect of including explicit water molecules on the absorption and emission spectra, is further discussed in the Supporting Information (SI).

Based on our quantum-chemical calculations, we conclude that the two electronic states, S_1 (red) and S_2 (green) states in Fig. 4 are responsible for the lowest-energy absorption band, located at about 4.80 eV (258 nm); experimentally at 4.86 eV (255 nm), while the S_3 (brown) and S_4 (violet) excited states contribute mostly to the higher energy region (5.78 eV, 215 nm; experimentally 5.93 eV, 209 nm). Based on our previous vertical excitation energies calculation with the ASEC-FEG approach, we can ascribe that these two bands are characterized by a $^1(\pi\pi^*)$ character.

Photochemical relaxation pathways. Vacuum. As shown in Table 3, following excitation at 267 nm, the S_1 $^1(\pi_7\pi_1^*)$ electronic state is populated. The most probable photophysical deactivation pathway is investigated using the MEP technique, computed at the XMS(2)-CASPT2 (10, 12)/cc-pVDZ level of theory, averaging over the two lowest lying singlet states (ground and S_1 $^1(\pi_7\pi_1^*)$), with the full π-space in the active space. It is essential to keep in mind that the MEP calculations at this level of theory demand a high computational effort because the nuclear gradients are computed numerically. The energies of the low-lying electronic states were recalculated at the XMS(4)-CASPT2 (12, 16)/cc-pVDZ at each optimized structure obtained from MEP calculation. The choice of this level of theory to recalculate the energies is because we can reproduce the results of higher active spaces (see Table S1), but at a reasonable computational cost. The final MEP is displayed in Fig. 5, showing that the S_1 $^1(\pi_7\pi_1^*)$ state evolves along a barrierless path from the Franck-Condon region (4.96 eV) toward the S_1 $^1(\pi_7\pi_1^*)_{min}^{MEP}$ region, at about 4.38 eV adiabatically bellow the initial region.

To verify whether the S_1 $^1(\pi_7\pi_1^*)_{min}^{MEP}$ region corresponds to a minimum in the S_1 $^1(\pi_7\pi_1^*)$ potential energy hypersurface (S_1 $^1(\pi_7\pi_1^*)_{min}$), the geometry of the S_1 $^1(\pi_7\pi_1^*)$ state was optimized at the XMS(2)-CASPT2 (10, 12)/cc-pVDZ level of theory. Afterward, the S_1 $^1(\pi_7\pi_1^*)_{min}^{MEP}$ and S_1 $^1(\pi_7\pi_1^*)_{min}$ regions were connected *via* a LIIC scan, computing the energy of each point along the interpolated pathway (Fig. 6) at the XMS(4)-CASPT2 (12, 16)/cc-pVDZ level of theory. At this level of theory, the S_1 $^1(\pi_7\pi_1^*)_{min}$ is located about 286 nm (4.34 eV) adiabatically above the ground state minimum.

As it can be noticed in Fig. 6, the LIIC interpolated pathway connecting the S_1 $^1(\pi_7\pi_1^*)_{min}^{MEP}$ and S_1 $^1(\pi_7\pi_1^*)_{min}$ regions is barrierless, with both structures at the same energetic region. It is also interesting to observe that both minima structures are at about 0.6 eV below the S_1 $^1(\pi_7\pi_1^*)_{FC}$ structure (4.96 eV). Therefore, we can conclude that the primary photophysical event from the FC region is the barrierless evolution of the S_1 $^1(\pi_7\pi_1^*)$ excited-state population toward a minimum energy region (S_1 $^1(\pi_7\pi_1^*)_{min}$) on its potential energy hypersurface.

From the S_1 $^1(\pi_7\pi_1^*)_{min}$ region (adiabatically at 4.34 eV) two deactivation pathways can be foreseen; radiatively through fluorescence and nonradiatively through a S_1/S_0 internal conversion (IC). Fluorescence was computationally found to occur at about 464 nm (2.67 eV), in relatively good agreement with the experimentally observed broad fluorescence at 390 nm (3.18 eV) in all solvents investigated. The (S_1 $^1(\pi_7\pi_1^*)/S_0)_{SSCP}$ singlet-singlet SSCP (Fig. 6 region *ii-iii*), was optimized at the XMS(4)-CASPT2 (12, 16)/cc-pVDZ level of theory and was found to be located at about the same energetic region (4.98 eV, 249 nm) of the S_1 $^1(\pi_7\pi_1^*)$ state, as previously observed at the FC region (4.96 eV). The LIIC pathway between the S_1 $^1(\pi_7\pi_1^*)_{min}$ and (S_1 $^1(\pi_7\pi_1^*)/S_0)_{SSCP}$ regions exhibit an energetic barrier of about 0.8 eV (19.4 kcal·mol^{-1}). As energetic barriers obtained along LIIC pathways correspond to an upper bound limit to the predicted value using MEP, these results could suggest that the nonradiative decay to the ground state is a likely deactivation channel, as proposed by Seela *et al*. (78) In summary, according to our theoretical results, a competition between both radiative and nonradiative decay is expected. However, we cannot quantify which process will be the most efficient. Nonadiabatic dynamics simulations are one way to answer this question, but currently such calculations are limited to a few picoseconds, requiring a high computational cost. However, based on the experimental results reported in this study (Table 1), we can infer

Table 3. Electronic nature and spectroscopic parameters for the low-lying singlet states of ^{5N7C}G in water and 1-propanol (n-PrOH).

	Gas phase				PCM (H_2O)				PCM (n-PrOH)			
	ΔE	f	Char.	μ	ΔE	f	Char.	μ	ΔE	f	Char.	μ
S_0	0.00	–	$^1(\pi^2)$	6.5	0.00	–	$^1(\pi^2)$	9.2	0.00	–	$^1(\pi^2)$	9.0
S_1	5.03	0.212	$^1(\pi\pi^*)$	6.0	5.22	0.232	$^1(\pi\pi^*)$	8.7	5.22	0.231	$^1(\pi\pi^*)$	8.5
S_2	5.73	0.002	$^1(n\pi^*)$	4.1	6.15	0.002	$^1(n\pi^*)$	5.9	6.13	0.002	$^1(n\pi^*)$	5.7
S_3	5.93	0.003	$^1(n\pi^*)$	3.0	6.24	0.001	$^1(n\pi^*)$	6.3	6.22	0.001	$^1(n\pi^*)$	6.1
S_4	6.51	0.002	$^1(n\pi^*)$	3.1	7.12	0.000	$^1(n\pi^*)$	4.8	7.08	0.000	$^1(n\pi^*)$	4.7
	Gas phase				ASEC-FEG (H_2O)				ASEC-FEG (n-PrOH)			
	ΔE	f	Char.	μ	ΔE	f	Char.	μ	ΔE	f	Char.	μ
S_0	0.00	–	$^1(\pi^2)$	6.5	0.00	–	$^1(\pi^2)$	11.0	0.00	–	$^1(\pi^2)$	9.4
S_1	5.03	0.212	$^1(\pi\pi^*)$	6.0	5.00	0.291	$^1(\pi\pi^*)$	11.0	5.02	0.178	$^1(\pi\pi^*)$	9.1
S_2	5.73	0.002	$^1(n\pi^*)$	4.1	5.42	0.026	$^1(\pi\pi^*)$	14.5	5.58	0.139	$^1(\pi\pi^*)$	9.6
S_3	5.93	0.003	$^1(n\pi^*)$	3.0	6.09	0.003	$^1(n\pi^*)$	7.3	5.97	0.002	$^1(n\pi^*)$	6.1
S_4	6.51	0.002	$^1(n\pi^*)$	3.1	6.23	0.002	$^1(n\pi^*)$	9.6	6.06	0.001	$^1(n\pi^*)$	6.0

Vertical excitation energies (ΔE, eV) and oscillator strengths (f) computed at the XMS(5)-CASPT2 (13, 18)/cc-pVDZ level of theory; electronic dipole moments (μ, Debye) were computed at the SA(5)-CASSCF (13, 18)/cc-pVDZ level of theory. The active space includes the n_1, n_o and n_3 lone pairs and the π, π* molecular orbitals. Solvent effects were considered using the PCM and ASEC-FEG methodologies.

that the nonradiative decay will be the dominant mechanism because a low fluorescence was measured.

The photophysical events occurring after excitation to the S_2 $^1(n_O\pi_1^*)$ electronic state were also investigated due to convolution of the S_1 and S_2 electronic states in the lowest energy band of the absorption spectra. As shown in Figure S5 *i-ii*, the S_2 $^1(n_O\pi_1^*)$ electronic state evolves barrierlessly from the FC region toward a singlet-singlet crossing region with the lowest singlet state, $(S_2\ ^1(n_O\pi_1^*)/(S_1\ ^1(\pi_7\pi_1^*))_{SSCP}$, where the electronic population is transferred ultrafast and nonradiatively to the S_1 $^1(\pi_7\pi_1^*)$ electronic state. Afterward, the same deactivation mechanism discussed previously for the S_1 $^1(\pi_7\pi_1^*)$ takes place (Fig. 6*ii*, *iii*). Note, optimized geometries at each key location on the photophysical relaxation pathway are shown in Fig. 7, displaying significant differences in bond lengths and torsion angles. These differences in geometry are further discussed in the SI.

Solvation effects. As displayed in Table 3, compared with the values in vacuum, the PCM model predicts that excitation energies in water and 1-propanol are blue-shifted, but the energetic nature and order of the state are retained. As discussed above, importantly with the ASEC-FEG solvation model, the S_2 state in polar protic solvents changes in order, that is, exhibiting a $^1(\pi\pi^*)$ character. Solvent effects on the main photochemical deactivation pathway $(S_0 \rightarrow S_1\ ^1(\pi_7\pi_1^*)_{FC} \rightarrow S_1\ ^1(\pi_7\pi_1^*)_{min} \rightarrow (S_1\ ^1(\pi_7\pi_1^*)/S_0)_{SSCP})$ were also investigated with the PCM and ASEC-FEG methods (Fig. 8). Ground and excited state geometry optimizations were performed at the XMS(2)-CASPT2 (10, 12)/cc-pVDZ/PCM level of theory, with an active space including all π and π* orbitals, except the orbital located on the NH_2 moiety

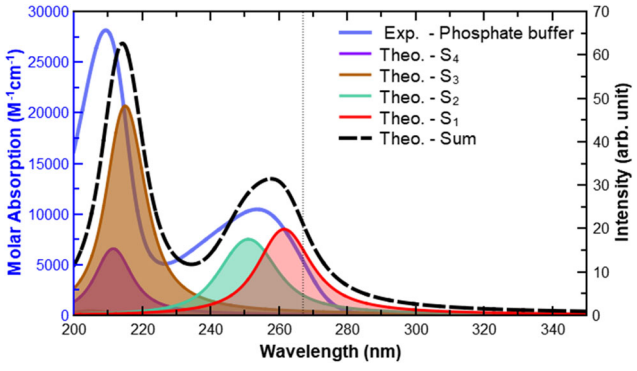

Figure 4. ^{5N7C}G absorption experimental (solid blue curve) and theoretical spectrum, obtained by the convolution of 100 statistically uncorrelated configurations, with vertical excitation energies computed at the XMS(7)-CASPT2 (14, 20)/cc-pVDZ/(7•H_2O) level of theory. The S_1–S_4 excitation contribution are represented in different colors (S_1: red; S_2: green; S_3: brown; S_4: violet). The spectrum was simulated by using a Lorentzian fit with an FWHM of 0.3 eV. The dotted line represents the excitation wavelength used in the time resolved experiments 267 nm.

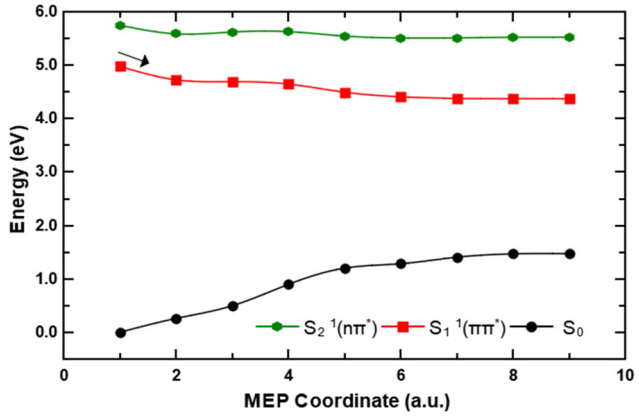

Figure 5. Energetic profiles of the ground, S_1 $^1(\pi_7\pi_1^*)$, and S_2 $^1(n_O\pi_1^*)$ electronic states from the Franck-Condon region (Point 1) toward the S_1 $^1(\pi_7\pi_1^*)_{min}^{MEP}$ region (Point 9), along with the minimum energy path on the S_1 $^1(\pi_7\pi_1^*)$ potential energy hypersurface, computed at the XMS(2)-CASPT2 (10, 12)/cc-pVDZ level of theory. Final vertical excitation energies at each point of the MEP were recomputed at the XMS(4)-CASPT2 (12, 16)/cc-pVDZ level of theory.

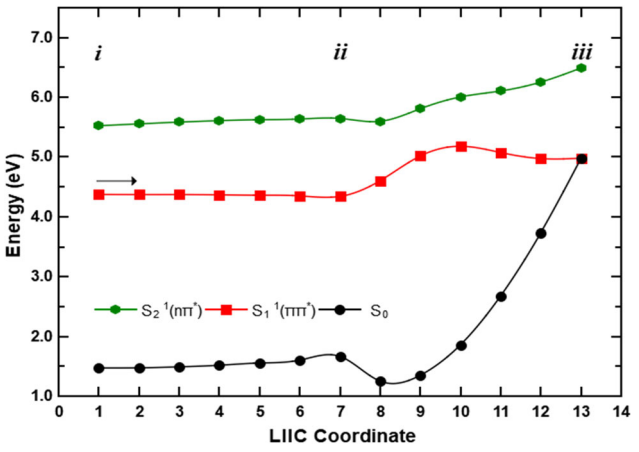

Figure 6. (i–ii) Linear interpolated (LIIC) energetic profiles of the ground, $S_1\ ^1(\pi_7\pi_1^*)$, and $S_2\ ^1(n_O\pi_1^*)$ electronic states from the $S_1\ ^1(\pi_7\pi_1^*)_{min}^{MEP}$ region toward the $S_1\ ^1(\pi_7\pi_1^*)_{min}$ region. (ii, iii) Linear interpolated pathway from the $S_1\ ^1(\pi_7\pi_1^*)_{min}$ region to the conical intersection with the ground state. Final vertical excitation energies at each point of the LIIC were computed at the XMS(4)-CASPT2 (12, 16)/cc-pVDZ level of theory.

(Figure S2). MECP structures were optimized at the XMS(4)-CASPT2 (12, 16)/cc-pVDZ/PCM level of theory, using the reaction field of the $S_1\ ^1(\pi_7\pi_1^*)$ excited state. Using the active space used for the vacuum optimizations, solvent effects calculations were carried out. Except for the ground state (S_0) geometry optimization with the ASEC-FEG method, which was done at the MP2/cc-pVDZ level of theory, the $S_1\ ^1(\pi_7\pi_1^*)_{min}$ geometry and $(S_1\ ^1(\pi_7\pi_1^*)/S_0)_{SSCP}$ structures were obtained at the same electronic structure level used for the calculations with the PCM model.

Solvation effects on the primary deactivation route, as described by the PCM method, do not differ much from those obtained in vacuum as it can be seen in Fig. 8 (left). Either with water or 1-propanol, the $S_1\ ^1(\pi_7\pi_1^*)$ state evolves barrierlessly from the FC region toward the minimum energy region on its potential energy hypersurface ($S_1\ ^1(\pi_7\pi_1^*)_{min}$), from where an energetic barrier of about 0.82 eV (against 0.84 eV in vacuum) must be overcome to reach the MECP structure with the ground state.

In contrast to findings in vacuum and the PCM method, we notice two significant changes when solvation effects are described with the ASEC-FEG method. First, the $S_1\ ^1(\pi_7\pi_1^*)$ hypersurface is well-defined in water and has a deep minimum (Fig. 8 top-right), while the hypersurface in 1-propanol solution (Fig. 8 bottom-right) is more scattered. This trend can be attributed to the molecular force field that describes the 1-propanol solution based on a three-center model. Finally, the $S_1\ ^1(\pi_7\pi_1^*)_{min}$ to $(S_1\ ^1(\pi_7\pi_1^*)/S_0)_{SSCP}$ conical intersection and the energetic barrier position depend on the solvent effects. The conical intersection is located vertically at 5.18 eV and 4.43 eV in water and 1-propanol, respectively. The estimated barriers (Path *ii–iii*) increase by 0.46 eV in water (1.28 eV; 29.52 kcal·mol^{-1}) and by 0.5 eV in 1-propanol (1.32 eV; 30.44 kcal·mol^{-1}), compared with the barrier calculated in vacuum (0.84 eV; 19.37 kcal·mol^{-1}). In water, the peak of the barrier is below the vertical excitation energy at the FC region (5.00 eV), but the conical intersection is placed at the same energy region. In propanol, the peak of the barrier is 0.35 eV higher than that obtained in the FC region (5.02 eV), and the conical intersection is 0.59 eV below. As the LIIC scan commonly overestimated the barriers, we might deduce that a portion of the population may reach the conical intersection in both solvents and return to the ground state in a nonradiative process. Importantly, as similarly described above in vacuum, deactivation from the $S_2\ ^1(\pi\pi^*)$ excited state in aqueous solution using the ASEC-FEG solvation model results in ultrafast and nonradiative transfer to the $S_1\ ^1(\pi_7\pi_1^*)$ electronic state (Figure S6).

Simulated absorption spectra (ESA) (Figure S15) from the $S_1\ ^1(\pi_7\pi_1^*)_{min}$ and $(S_1\ ^1(\pi_7\pi_1^*)/S_0)_{SSCP}$ regions were also emulated at the XMS(10)-CASPT2 (13, 18)/cc-pVDZ level of theory in vacuum, water and 1-propanol. In both solvents, the solvent was treated either with the PCM or ASEC-FEG methods. It is important recalling that the computation of these spectra requires a state-averaged procedure with many to cover the experimental window, which can lower the expected accuracy of the method. Nonetheless, when solvent molecules are included explicitly, the computed spectra are shift by about 50 nm in comparison with the experimental ones, indicating a good agreement between the experimental and theoretical results.

DISCUSSION

As shown in Fig. 1, the lowest energy absorption band maximally absorbs at *ca.* 255 nm, irrespective of solvent polarity. These results are in accordance with the theoretically obtained

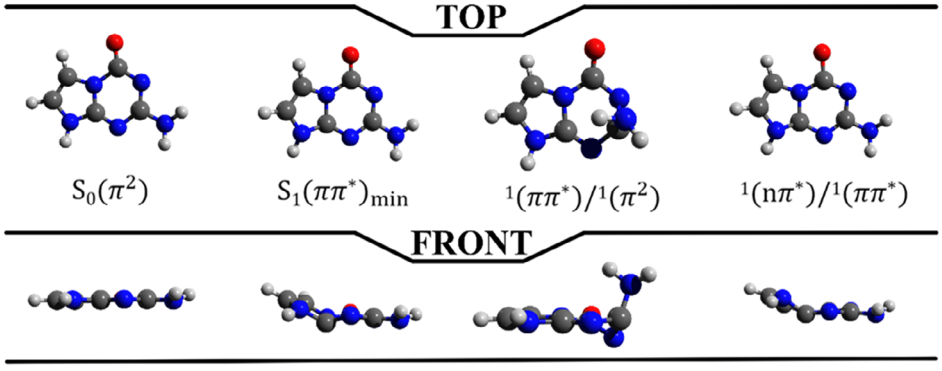

Figure 7. Top and frontal views of ^{5N7C}G vacuum ground state $(S_0\ (\pi^2)_{min})$, $(S_1\ ^1(\pi_7\pi_1^*)_{min})$, $(S_1\ ^1(\pi_7\pi_1^*)/S_0)_{SSCP}$ and $(S_2\ ^1(n_O\pi_1^*)/(S_1\ ^1(\pi_7\pi_1^*))_{SSCP}$ optimized structures. $(S_0\ (\pi^2)_{min})$, $S_1\ ^1(\pi_7\pi_1^*)_{min}$, $(S_1\ ^1(\pi_7\pi_1^*)/S_0)_{SSCP}$ and $(S_2\ ^1(n_O\pi_1^*)/(S_1\ ^1(\pi_7\pi_1^*))_{SSCP}$ were optimized, respectively, at the XMS(4)-CASPT2 (13, 18)/cc-pVDZ, XMS(2)-CASPT2 (10, 12)/cc-pVDZ and XMS(4)-CASPT2 (12, 16)/cc-pVDZ levels of theory.

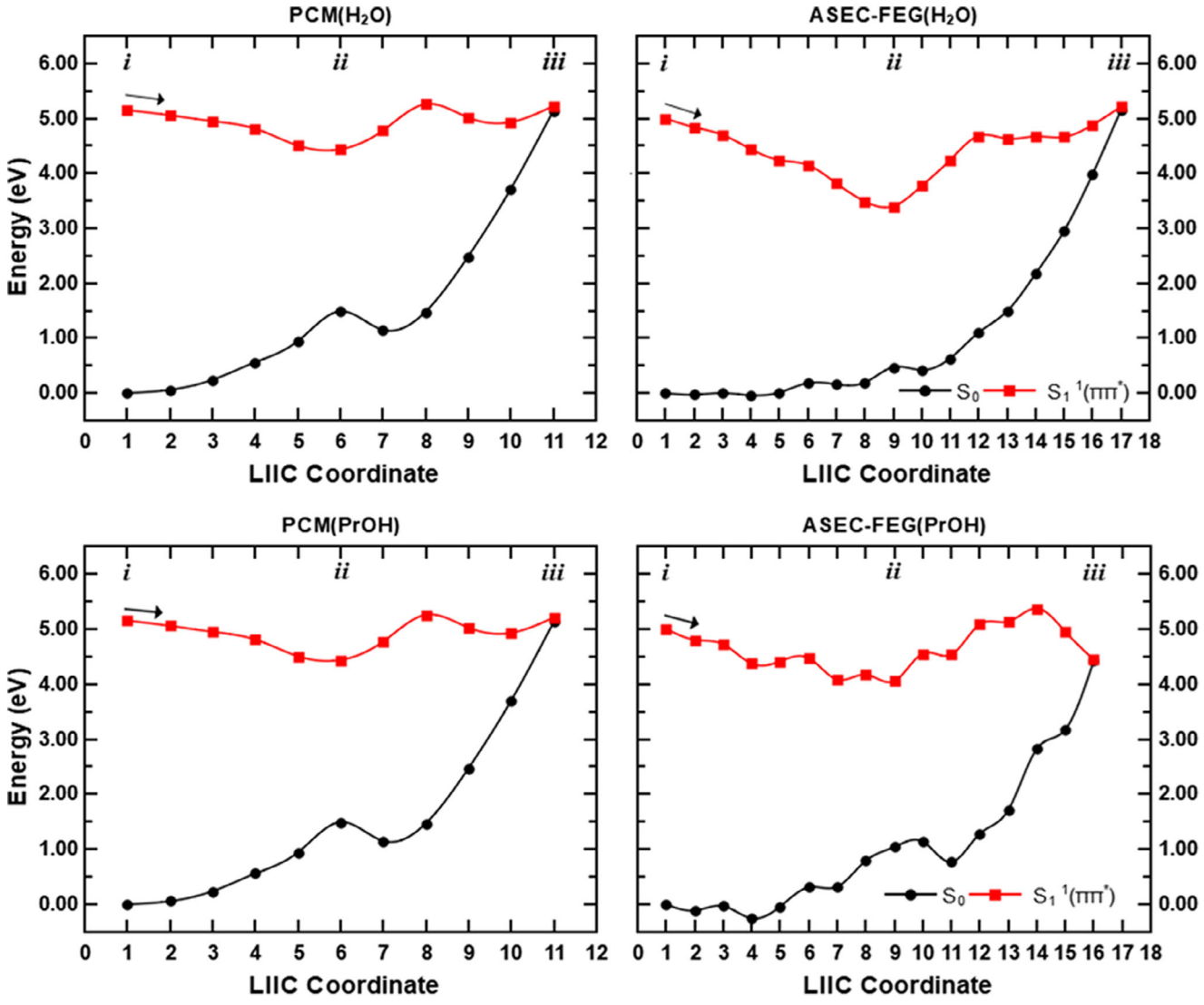

Figure 8. ^{5N7C}G linear interpolated pathways connecting the S_0 to S_1 $^1(\pi_7\pi_1^*)_{min}$ (i to ii) and from S_1 $^1(\pi_7\pi_1^*)_{min}$ to $(S_1$ $^1(\pi_7\pi_1^*)/S_0)_{SSCP}$ singlet-singlet crossing point (ii to iii). Vertical energies were carried out at XMS(5)-CASPT2 (13, 18)/cc-pVDZ level of theory in aqueous (top) and 1-propanol (bottom) solutions. Energies with the PCM model were obtained with the reaction field of the bright state at left and ASEC-FEG protocol at right. The active space consists of n_1, n_2 and n_3 lone pairs and the set of π molecular orbitals.

vertical excitation energies (Table 2) computed at the XMS(7)-CASPT2 (14, 20)/cc-pVDZ level of theory. The lowest energy absorption band is proposed to be composed of both S_1 and S_2 electronic states, as shown in Figure S7, suggesting that a combination of both states is populated following excitation at 267 nm.

Importantly, the character of the S_2 state varies depending on the solvation model used. Specifically, in vacuum and water, as described by the PCM model, the S_2 is characterized as an nπ* transition; but the ASEC-FEG method predicts that in water, the S_2 state is characterized as a ππ* state. This is significant because transitions from the ground to $^1(\pi\pi^*)$ state are expected to have considerably more oscillator strengths and, therefore, a higher probability of direct population upon irradiation. Regardless of the solvation model used, however, the energy gap between the lowest lying $^1(\pi\pi^*)$ and $^1(n\pi^*)$ states are found to increase with increase in solvent polarity (Table 3), showing destabilization of the $^1(n\pi^*)$ state in water and in PrOH. The ASEC-FEG is a QM/MM model that uses an average electrostatic embedding to describe the solvent–solute interaction. Hence, it should yield a more accurate representation of the solvation effects than relying mainly on the bulk dielectric constant of the solvent, as it is done in the PCM approach. Therefore, we propose that the S_2 state has a ππ* character in water and PrOH, whereas it should have an nπ* character in ACN'.

Using a linear combination of two Gaussian functions to model the absorption spectrum of the lowest energy band from 230 nm to 310 nm (Figure S2), it is estimated that about 90% of the initially excited population reaches the S_1 $^1(\pi\pi^*)$ state and about 10% reaches the S_2 $^1(\pi\pi^*)$ in water and in PrOH' (about 10% reaches the nπ* state in ACN', see Eq. S1). Regarding direct population of the ^{1}nπ* state in ACN', our results (Table S1) predicts that the oscillator strength associated with this state is very small (~0.003), but it is not null. Therefore, this finding predicts that a negligible fraction of molecules may directly reach to the nπ* state.

We are now in a favorable position to assign the transient absorption spectra of ^{5N7C}G on each solvent. The black EADS1, observed within the time resolution of the instrument, is assigned to a combination of absorption spectra from both the S_1 and S_2 states (*i.e.* S_1 $^1(\pi\pi^*)$ and S_2 $^1(\pi\pi^*)$ states in water and in PrOH', and S_1 $^1(\pi\pi^*)$ and S_2 $^1(n\pi^*)$ states in ACN'). Following Kasha's rule (79), the population excited to the higher energy S_2 state is expected to internally convert to the lower energy S_1 $^1(\pi_7\pi_1^*)$ state. This nonradiative process is thought to occur on an ultrafast time scale, <100 fs, as reported for the guanine monomers (24,80–82). Similarly, quick internal conversion from the $^1n\pi^*$ state to the lower-lying $^1\pi\pi^*$ state in ACN' is supported by LIIC pathway calculated in vacuum (Figure S5), which shows barrierless access to a $(S_2\ ^1(n_O\pi_1^*)/(S_1\ ^1(\pi_7\pi_1^*))_{SSCP}$ MECP near the FC region.

Like the pathway calculated in vacuum, we also obtained the deactivation route of the second excited state (S_2 $^1(\pi\pi^*)$) in water using the ASEC-FEG protocol (Figure S6). The most interesting aspect is the evolution of the molecular geometry in a barrierless path from the FC region (point 1) toward the minimum of the bright state (S_1 $^1(\pi_7\pi_1^*)_{min}$; point 17). As shown in Figure S6, the results evidence that after the absorption process, the electronic population of the S_2 $^1(\pi\pi^*)$ state might be transferred directly to the S_1 $^1(\pi\pi^*)$ state efficiently through a nonradiative mechanism due to easy access the $(S_2\ ^1(\pi\pi^*)/S_1\ ^1(\pi\pi^*))_{SSCP}$ crossing point, computed to be, at the XMS(5)-CASPT2 (13, 18)/cc-pVDZ level of theory, 5.17 eV vertically above the ground state. The S_2 $^1(\pi\pi^*)$ state hypersurface has no minimum because the geometry optimization in aqueous solution along with this state leads to the crossing point region, which is consistent with Figure S6. The simulated transient absorption spectra of the $(S_2\ ^1(\pi\pi^*)/S_1\ ^1(\pi\pi^*))_{SSCP}$ minimum energy geometry in an aqueous solution can be observed in Figure S8.

Following internal conversion to the S_1 $^1(\pi_7\pi_1^*)$ state, the excited state population is proposed to traverse toward a local minimum. Hence, internal conversion from the S_2 to the S_1 $^1(\pi_7\pi_1^*)$ state, and the initial movement along the S_1 $^1(\pi_7\pi_1^*)$ PES occur within the first lifetime of *ca.* 0.3 ± 0.1 ps (Table 2). The red EADS2 is assigned to the vibrationally excited S_1 $^1(\pi_7\pi_1^*)$ state (Fig. 3). This corresponds well with the simulated excited state absorption spectra (Figure S15a,c,e). The excited population in the S_1 $^1(\pi_7\pi_1^*)$ state is proposed to undergo an intramolecular conformational change while traversing to a local minimum, associated to the second lifetime reported in Table 1. The intramolecular conformational relaxation is supported by the blue shift and band narrowing observed in the transient absorption spectra (Fig. 2). Interestingly, this lifetime shows a slight dependence on the identity of solvent, suggesting that intermolecular energy relaxation (*i.e.* solvation dynamics) also takes place. In each solvent, the molecular geometry is going from planar to puckered with $C_7N_5C_4N_3$ and $C_6N_5C_4N_9$ torsion angles between the pyrimidine and imidazole ring of −120.4° and 154.0°, respectively (Fig. 7). The similar geometries in the FC region and in the S_1 $^1(\pi_7\pi_1^*)_{min}$ in each solvent helps support the values obtained for τ_2 being of the same order of magnitude, where the lifetime also increases with increased solvent–solute interaction. This significant geometric change agrees well with the large stokes shift observed between the ground state absorption and fluorescence emission (Figure S1). The S_1 minimum is therefore associated with EADS3 in Fig. 3(d–f).

From the S_1 minimum (Fig. 6), the excited state population is proposed to bifurcate. A portion of the population decays radiatively *via* fluorescence with a fluorescence quantum yield ranging from 0.4×10^{-3} to 1.8×10^{-3} in going from phosphate buffer to PrOH' solvent, whereas the other portion decays nonradiatively to the ground electronic state mediated by a $(S_1\ ^1(\pi_7\pi_1^*)/S_0)_{SSCP}$ MECP. This combination of relaxation processes is associated with the third average lifetime, τ_3, which importantly shows significant solvent specificity, with water being the fastest and PrOH' the slowest. The order of magnitude of the fluorescence quantum yield is similar for each solvent (Table 1), suggesting the lifetime of the S_1 $^1(\pi_7\pi_1^*)$ state should be of similar magnitude. This hypothesis is further supported in Figure S9a, which shows the band in the visible, assigned to the $S_1{}^1(\pi_7\pi_1^*)$ state, decays at the same rate within the signal-to-noise in the three solvents investigated.

The fluorescence decay from the S_1 $^1(\pi_7\pi_1^*)_{min}$, however, cannot be deconvoluted from the excited state population decaying *via* internal conversion through the $(S_1\ ^1(\pi_7\pi_1^*)/S_0)_{SSCP}$. The latter is associated to the UV edge of the probing window in EADS 3 (Fig. 3d–f). The difference in rates of nonradiative decay between solvents is emphasized in Figure S3b. It should be noted that the nonradiative decay through the $(S_1\ ^1(\pi_7\pi_1^*)/S_0)_{SSCP}$ is proposed to be the rate-limiting step in ACN' and PrOH', but not in aqueous solution, as shown by the slower rate of decay in the UV region compared with the visible region (Figure S10). Furthermore, there is an energy barrier from the S_1 $^1(\pi_7\pi_1^*)_{min}$ to the $(S_1\ ^1(\pi_7\pi_1^*)/S_0)_{SSCP}$ of approximately 0.84 eV in a vacuum (Fig. 6) and 0.82 eV in water and PrOH using the PCM model (Fig. 8) at the XMS(5)-CASPT2 (13, 18)/cc-pVDZ level of theory. Notably, when solvation was implemented using the ASEC-FEG method, the estimated energy barrier increased to 1.28 eV in water and 1.32 eV in PrOH (Fig. 8). The difference in magnitudes of the energetic barrier required to access the $(S_1\ ^1(\pi_7\pi_1^*)/S_0)_{SSCP}$ in a vacuum, water and PrOH further lends support that the lifetime associated with this process increases with solvent, with PrOH being the longest. In relaxing from the $(S_1\ ^1(\pi_7\pi_1^*)/S_0)_{SSCP}$ back to the S_0 minimum, ^{5N7C}G must go from a C_2-puckered, C_2-N_3 ethylenic twisted conformation back to a

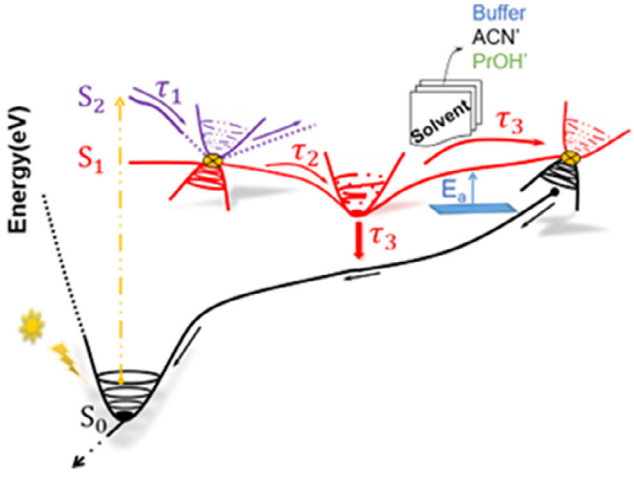

Scheme 1. Proposed electronic relaxation mechanism for ^{5N7C}G. The conical intersections are indicated by the black X inside the yellow circle.

relaxed planar geometry (Fig. 7). It is hypothesized that London dispersion forces arising from the aliphatic chains between propanol molecules and rigidity in acetonitrile molecules might slow down (drag) this geometric relaxation, thus contributing to the longer τ_3 values compared with water. We summarize the proposed electronic relaxation pathways of ^{5N7C}G in the three solvents in Scheme 1.

CONCLUSIONS

In this paper, 5-aza-7-deazaguanine was studied to investigate the effect of atom substitution on the relaxation mechanism, compared with the canonical guanine nucleobase. The investigated atom exchange was unique, as it disturbed not only the integrity of the purine imidazole but also that of the pyrimidine $C_5 = C_6$ ethylenic bond. The distinct N_5 amine can adopt a trigonal planar (sp^2) or tetrahedral (sp^3) hybridization during relaxation, allowing for increased degrees of freedom, giving rise to the conformation changes observed in the experimental and computational results relative to guanine.

Following excitation to the lowest energy $^1\pi\pi^*$ state, it is demonstrated that complex dynamics occur, resulting in slower relaxation compared with guanine. A significant conformational change occurs between the planar Franck-Condon geometry and the S_1 minimum, resulting in a 10-fold greater fluorescence quantum yield and *ca*. 10- to 30-fold increase in excited state lifetime relative to guanine (24,80,81,83). Both the fluorescence quantum yield and S_1 decay lifetime were found to increase with increased solvent size or molecular weight (*i.e*. water < ACN < PrOH). These results were supported by static mapping of the relaxation pathway showing a difference in energetic barrier height between the S_1 minimum and S_1/S_0 conical intersection for each solvent. Again, a significant conformational change was found between the S_1 minimum and S_1/S_0 conical intersection, further lending support to the longer decay lifetime in the order of tens of picoseconds. Ultimately, while the excited singlet state does fully decay back to the ground state, the increased lifetimes and fluorescence quantum yield compared with the canonical guanine nucleobase, or other nucleobases, might make this guanine derivative more prone to photochemical reaction to adjacent nucleobases than guanine (or other nucleobases) within DNA.

Acknowledgements—S.E.K., S.J.H. and C.E.C.H. acknowledge funding from the National Science Foundation (Grant No. CHE-1800052). G.J.C. thanks CAPES (Coordenação de Aperfeiçoamento de Pessoal de Nível Superior) for research fellowship (Project number 88882.328213/2019-01). D. V. acknowledges funding from the Fonds de la Recherche Scientifiques de Belgique (F.R.S.-FNRS) under the grant F.4534.21 (MIS-IMAGINE). L.M.F.O. thanks CAPES for research fellowship (Project number 88882.328237/2019-01). A.C.B. thanks CNPq (Conselho Nacional de Desenvolvimento Científico e Tecnológico) for research fellowship (project number 311821/2021-9) and FAPESP (Fundação de Amparo à Pesquisa do Estado de São Paulo) for the research grant. The authors acknowledge the services and compute time provided by the Superintendência de Tecnologia da Informação da Universidade de São Paulo.

SUPPORTING INFORMATION

Additional supporting information may be found online in the Supporting Information section at the end of the article:

Appendix S1. Supporting Information.

Figure S1. Normalized steady-state absorption and emission spectra of 5-aza-7-deazaguanine in phosphate buffer pH 6.8 (a), 90% acetonitrile mixed with 10% ultrapure water (ACN', b) and 90% 1-propanol mixed with 10% ultrapure water (PrOH', c).

Methods S1. Computational methods.

Figure S2. 5-Aza-7-deazaguanine average valence natural orbitals computed at the SA(4)-CASSCF (14, 20)/cc-pVDZ level of theory at the ground state optimized geometry. The π1 orbital localized on the amino group (NH2) is inactive because it is always doubly occupied in the gas phase. Atomic labels are shown in the inset.

Table S1. Vertical excitation energy (Δ*E*, eV/nm), oscillator strength (f) and electric dipole moments (μ, Debye) for the three low-lying singlet states of 5-aza-7-deazaguanine in gas phase computed averaging over the different number of states (X). The active space encompasses Y electrons distributed over Z orbitals (XMS(X)-CASPT2(Y, Z); see Figure S5). Electric dipole moments were computed at the corresponding SA(X)-CASSCF (Y, Z)/cc-pVDZ level of theory.

Table S2. 5N7CG maxima absorption (λλmmaaaamm) and emission bands (λλeemmmmaaeemm), and the corresponding Stokes shifts, in water and 1-propanol (PrOH). Vertical excitation energies were computed at the XMS(5)-CASPT2(18,13)/cc-pVDZ level of theory, and solvent effects were considered with the PCM and ASEC-FEG methods. The active space consists of n1, n2, and n3 lone pairs and the set of π and π* molecular orbitals (except the π located on the NH2 moiety). Excitation energies are reported in eV (nm in parenthesis).

Figure S3. 5N7CG absorption spectrum in phosphate buffer pH 6.8 (blue), 90 % acetonitrile mixed with 10% ultrapure water (black), and 90% 1-propanol mixed with 10% ultrapure water (green). A theoretical absorption spectrum (dashed red) is also displayed, and it is obtained by convoluting 100 statistically uncorrelated configurations, with vertical excitation energies computed at the XMS(7)-CASPT2(20,14)/cc-pVDZ/(7 H2O) level of theory. The spectrum was simulated by employing a Lorentzian fit with an FWHM of 0.3 eV. The vertical dashed line represents the experimental excitation at 267 nm.

Table S3. Mean values (Δ*E*) and standard deviations of the vertical absorption and their associated oscillator strength (f) as well as the emission energies (eV) for 5N7CG. Vertical energies were obtained at the XMS(7)-CASPT2(20,14)/cc-pVDZ level of theory. One hundred statistically uncorrelated configurations are considered in the total where the solute and the κ nearest water molecules are detailed quantum mechanically, and the remainder water molecules are treated as point charges. The number κ is seven for the ground state and nine for the S1 state.

Figure S4. ^{5N7C}G normalized emission spectrum obtained by the convolution of 100 statistically uncorrelated snapshots, with vertical emission energies calculated at XMS(7)-CASPT2 (14, 20)/cc-pVDZ level of theory. Nine water molecules were treated with quantum mechanics, and the remaining ones were as point charges. This spectrum is emulated *via* a sum of Lorentzian functions with an FWHM of 0.3 eV.

Figure S5. (i-ii) Linear interpolated pathway between the S_2 $^1(n_O\pi_1^*)$ (point 1) and the S_2 $^1(n_O\pi_1^*)/(S_1$ $^1(\pi_7\pi_1^*))_{SSCP}$ (point 6) singlet-singlet crossing point; (ii–iii) LIIC interpolated pathway between the S_2 $^1(n_O\pi_1^*)/(S_1$ $^1(\pi_7\pi_1^*))_{SSCP}$ and the S_1 $^1(\pi_7\pi_1^*)$min region. In both cases, the energies for each LIIC structure were calculated at the XMS(5)-CASPT2 (13, 18)/cc-

pVDZ level of theory to maintain the consistency of the used active space in the LIIC scan.

Figure S6. 5N7CG linear interpolated pathways connecting the S2 1(ππ*) to (S2 1(ππ*)/S1 1(ππ*))SSCP singlet-singlet crossing point (*i-ii*), and from the crossing point to S1 1(π7π1*) min (*ii–iii*). Vertical energies were carried out at XMS(5)-CASPT2(18,13)/cc-pVDZ level of theory in aqueous obtained with ASEC-FEG protocol. The active space consists of n1, n2, and n3 lone pairs and the set of π molecular orbitals.

Figure S7. Deconvolution of the lowest energy absorption band of 5-aza-7-deazaguanine into the two lowest singlet states using a linear combination of two Gaussian functions. The vertical line shows the excitation wavelength of 267 nm.

Figure S8. Simulated transient absorption spectra for $(S_2\ ^1(\pi\pi^*)/S_1\ ^1(\pi\pi^*))_{SSCP}$ singlet-singlet crossing point of ^{5N7C}G, calculated at the XMS(10)-CASPT2 (13, 18)/cc-pVDZ level of theory in aqueous solution using the ASEC-FEG model.

Figure S9. Representative kinetic traces at probe wavelengths of 505 nm (a) and 350 nm (b).

Figure S10. Comparison on kinetic decay traces in the UV (350 nm) and visible region (505 nm) of 5-aza-7-deazaguanine in aqueous solution (a), ACN' (b) and PrOH' (c).

Figure S11. Minimum-distance pairwise distribution function for the ground (black) and $S_1\ ^1(\pi_7\pi_1^*)$ (red) states in water (p = 1 atm; T = 298 K).

Figure S12. Site-specific pairwise distribution function g(r) for the most electronegative atoms on the ground state (left) and $S_1\ ^1(\pi_7\pi_1^*)$ min state (right) in water (p = 1 atm; T = 298 K).

Figure S13. Mean value of the six lower excited states (straight line) in ascending order and their accumulated value (square) in terms of the number of considered snapshots (configurations). The vertical energies are computed at XMS(7)-CASPT2(20,14)/cc-pVDZ/(κ = 7 H2O) level of theory. The reference structure referred to the ground state geometry optimized in water employing the ASEC-FEG method.

Figure S14. Mean value of the six lower excited states (straight line) in ascending order and their accumulated value (square) in terms of the number of considered configurations (snapshots). The vertical emission energies are computed at XMS(7)-CASPT2(20,14)/cc-pVDZ/(κ = 9 H2O) level of theory. The reference structure referred to the lowest-lying singlet state geometry optimized in water employing the ASEC-FEG method.

Figure S15. Simulated absorption spectra (ESA) of the $S_1\ ^1(\pi_7\pi_1^*)$ minimum geometry (top) and $(S_1\ ^1(\pi_7\pi_1^*)/S_0)_{SSCP}$ (bottom) calculated at the XMS(10)-CASPT2 (13, 18)/cc-pVDZ level of theory in gas-phase (a, b), water (c, d) and 1-propanol (e, f).

REFERENCES

1. Travers, A. and G. Muskhelishvili (2015) DNA structure and function. *FEBS J.* **282**, 2279–2295.
2. Rich, A. (2009) The era of RNA awakening: Structural biology of RNA in the early years. *Q. Rev. Biophys.* **42**, 117–137.
3. Karikó, K., M. Buckstein, H. Ni and D. Weissman (2005) Suppression of RNA recognition by toll-like receptors: The impact of nucleoside modification and the evolutionary origin of RNA. *Immunity* **23**, 165–175.
4. Karijolich, J. and Y. T. Yu (2014) Therapeutic suppression of premature termination codons: Mechanisms and clinical considerations (review). *Int. J. Mol. Med.* **34**, 355–362.
5. Wickstrom, E. (2015) DNA and RNA derivatives to optimize distribution and delivery. *Adv. Drug Deliv. Rev.* **87**, 25–34.
6. Parr, C. J. C., S. Wada, K. Kotake, S. Kameda, S. Matsuura, S. Sakashita, S. Park, H. Sugiyama, Y. Kuang and H. Saito (2020) N 1-Methylpseudouridine substitution enhances the performance of synthetic mRNA switches in cells. *Nucleic Acids Res.* **48**, E35.
7. Boo, S. H. and Y. K. Kim (2020) The emerging role of RNA modifications in the regulation of mRNA stability. *Exp. Mol. Med.* **52**, 400–408.
8. Pollum, M., M. Lam, S. Jockusch and C. E. Crespo-Hernández (2018) Dithionated nucleobases as effective photodynamic agents against human epidermoid carcinoma cells. *ChemMedChem* **13**, 1044–1050.
9. Benner, S. A., H.-J. Kim and Z. Yang (2012) Setting the stage: The history, chemistry, and geobiology behind RNA. *Cold Spring Harb. Perspect. Biol.* **4**, a003541.
10. Beckstead, A. A., Y. Zhang, M. S. de Vries and B. Kohler (2016) Life in the light: Nucleic acid photoproperties as a legacy of chemical evolution. *Phys. Chem. Chem. Phys.* **18**, 24228–24238.
11. Cafferty, B. J. and N. V. Hud (2015) Was a pyrimidine-pyrimidine Base pair the ancestor of Watson-Crick Base pairs? Insights from a systematic approach to the origin of RNA. *Isr. J. Chem.* **55**, 891–905.
12. Kitadai, N. and S. Maruyama (2018) Origins of building blocks of life: A review. *Geosci. Front.* **9**, 1117–1153.
13. Rios, A. C. and Y. Tor (2013) On the origin of the canonical nucleobases: An assessment of selection pressures across chemical and early biological evolution. *Isr. J. Chem.* **53**, 469–483.
14. Hud, N. V., B. J. Cafferty, R. Krishnamurthy and L. D. Williams (2013) The origin of RNA and 'my grandfather's axe'. *Chem. Biol.* **20**, 466–474.
15. Hoehn, S. J., N. E. Caldero-Rodríguez and C. E. Crespo-Hernández (2021) Chapter 9. Photochemistry of RNA, RNA monomers, and plausible prebiotic precursors. In *DNA Photodamage: From Light Absorption to Cellular Responses and Skin Cancer*, pp. 197–226. The Royal Society of Chemistry, Croydon, UK. https://doi.org/10.1039/9781839165580-00197
16. Schmidt, M. (2010) Xenobiology: A new form of life as the ultimate biosafety tool. *BioEssays* **32**, 322–331.
17. Nie, P., Y. Bai and H. Mei (2020) Synthetic life with alternative nucleic acids as genetic materials. *Molecules* **25**, 3483.
18. Biondi, E. and S. A. Benner (2018) Artificially expanded genetic information systems for new aptamer technologies. *Biomedicine* **6**, 1–13.
19. Lee, K. H., K. Hamashima, M. Kimoto and I. Hirao (2018) Genetic alphabet expansion biotechnology by creating unnatural base pairs. *Curr. Opin. Biotechnol.* **51**, 8–15.
20. Huttert, D. and S. A. Benner (2003) Expanding the genetic alphabet: Non-epimerizing nucleoside with the pyDDA hydrogen-bonding pattern. *J. Org. Chem.* **68**, 9839–9842.
21. Pollum, M., B. Ashwood, S. Jockusch, M. Lam and C. E. Crespo-Hernández (2016) Unintended consequences of expanding the genetic alphabet. *J. Am. Chem. Soc.* **138**, 11457–11460.
22. Hoshika, S., N. A. Leal, M.-J. Kim, M.-S. Kim, N. B. Karalkar, H. Kim, A. M. Bates, N. E. Watkins, H. A. SantaLucia, A. J. Meyer, S. DasGupta, J. A. Piccirilli, A. D. Ellington, J. SantaLucia, M. M. Georgiadis and S. A. Benner (2019) Hachimoji DNA and RNA: A genetic system with eight building blocks. *Science* **363**, 884–887.
23. Dziuba, D., P. Didier, S. Ciaco, A. Barth, C. A. M. Seidel and Y. Mély (2021) Fundamental photophysics of isomorphic and expanded fluorescent nucleoside analogues. *Chem. Soc. Rev.* **50**, 7062–7107.
24. Krul, S. E., S. J. Hoehn, K. J. Feierabend and C. E. Crespo-Hernández (2021) Excited state dynamics of 7-deazaguanosine and guanosine 5′-monophosphate. *J. Chem. Phys.* **154**, 075103.
25. Kim, S., D. G. Bartholomew, L. B. Allen, R. K. Robins, G. R. Revankar and P. Dea (1978) Imidazo[1,2-a]-s-triazine nucleosides. Synthesis and antiviral activity of the N-bridgehead guanine, guanosine, and guanosine monophosphate analogs of imidazo[1,2-a]-s-triazine. *J. Med. Chem.* **21**, 883–889.
26. Kobayashi, T., H. Kuramochi, Y. Harada, T. Suzuki and T. Ichimura (2009) Intersystem crossing to excited triplet state of aza analogues of nucleic acid bases in acetonitrile. *J. Phys. Chem. A* **113**, 12088–12093.
27. Sanches De Araújo, A. V. and A. C. Borin (2019) Photochemical relaxation pathways of 9 H-8-azaguanine and 8 H-8-azaguanine. *J. Phys. Chem. A* **123**, 3109–3120.

28. Fang, Y.-G., D. Valverde, S. Mai, S. Canuto, A. C. Borin, G. Cui and L. González (2021) Excited-state properties and relaxation pathways of selenium-substituted guanine nucleobase in aqueous solution and DNA duplex. *J. Phys. Chem. B* **125**, 1778–1789.
29. McKenzie, L. K., R. El-Khoury, J. D. Thorpe, M. J. Damha and M. Hollenstein (2021) Recent progress in non-native nucleic acid modifications. *Chem. Soc. Rev.* **50**, 5126–5164.
30. Saito, Y. and R. H. E. Hudson (2018) Base-modified fluorescent purine nucleosides and nucleotides for use in oligonucleotide probes. *J. Photochem. Photobiol. C: Photochem. Rev.* **36**, 48–73.
31. Caldero-Rodríguez, N. E., E. M. Arpa, D. J. Cárdenas, L. Martínez-Fernández, S. Jockusch, S. K. Seth, I. Corral and C. E. Crespo-Hernández (2022) 2-Oxopurine riboside: A dual fluorescent analog and photosensitizer for RNA/DNA research. *J. Phys. Chem. B* **126**, 4483–4490.
32. Ashwood, B., S. Jockusch and C. E. Crespo-Hernández (2017) Photochemical reactivity of dTPT3: A crucial nucleobase derivative in the development of semisynthetic organisms. *J. Phys. Chem. Lett.* **8**, 2387–2392.
33. Ashwood, B., M. Pollum and C. E. Crespo-Hernández (2016) Can a six-letter alphabet increase the likelihood of photochemical assault to the genetic code? *Chem. Eur. J.* **22**, 16648–16656.
34. Middleton, C. T., K. de La Harpe, C. Su, Y. K. Law, C. E. Crespo-Hernández and B. Kohler (2009) DNA excited-state dynamics: From single bases to the double helix. *Annu. Rev. Phys. Chem.* **60**, 217–239.
35. Schreier, W. J., P. Gilch and W. Zinth (2015) Early events of DNA photodamage. *Annu. Rev. Phys. Chem.* **66**, 497–519.
36. Zhong, D. (2015) Electron transfer mechanisms of DNA repair by photolyase. *Annu. Rev. Phys. Chem.* **66**, 691–715.
37. Berg, J. M., J. L. Tymoczko and L. Stryer (2011) *Biochemistry*, 7th ed. W.H. Freeman and Company, New York, NY.
38. Sugasawa, K. (2019) Mechanism and regulation of DNA damage recognition in mammalian nucleotide excision repair. *Enzyme* **45**, 99–138.
39. Li, L. Y., Y. Guan, X. S. Chen, J. M. Yang and Y. Cheng (2021) DNA repair pathways in cancer therapy and resistance. *Front. Pharmacol.* **11**, 1–13.
40. Zhao, B., E. Rothenberg, D. A. Ramsden and M. R. Lieber (2020) The molecular basis and disease relevance of non-homologous DNA end joining. *Nat. Rev. Mol. Cell Biol.* **21**, 765–781.
41. Chang, H. H. Y., N. R. Pannunzio, N. Adachi and M. R. Lieber (2017) Non-homologous DNA end joining and alternative pathways to double-strand break repair. *Nat. Rev. Mol. Cell Biol.* **18**, 495–506.
42. Yi, C. and C. He (2013) DNA repair by reversal of DNA damage. *Cold Spring Harb. Perspect. Biol.* **5**, a012575.
43. Dien, V. T., M. Holcomb and F. E. Romesberg (2019) Eight-letter DNA. *Biochemistry* **58**, 2581–2583.
44. Jean, J. M. and K. B. Hall (2001) 2-Aminopurine fluorescence quenching and lifetimes: Role of base stacking. *Proc. Natl. Acad. Sci. USA* **98**, 37–41.
45. Reichardt, C., C. Wen, R. A. Vogt and C. E. Crespo-Hernández (2013) Role of intersystem crossing in the fluorescence quenching of 2-aminopurine 2′-deoxyriboside in solution. *Photochem. Photobiol. Sci.* **12**, 1341–1350.
46. Ashwood, B., M. Pollum and C. E. Crespo-Hernández (2019) Photochemical and photodynamical properties of sulfur-substituted nucleic acid bases. *Photochem. Photobiol.* **95**, 33–58.
47. Nguyen, V. N., Y. Yan, J. Zhao and J. Yoon (2021) Heavy-atom-free photosensitizers: From molecular design to applications in the photodynamic therapy of cancer. *Acc. Chem. Res.* **54**, 207–220.
48. Ortiz-Rodríguez, L. A., C. Reichardt, S. J. Hoehn, S. Jockusch and C. E. Crespo-Hernández (2020) Detection of the thietane precursor in the UVA formation of the DNA 6-4 photoadduct. *Nat. Commun.* **11**, 3599.
49. Brister, M. M., T. Gustavsson and C. E. Crespo-Hernández (2020) Excited state lifetimes of sulfur-substituted DNA and RNA monomers probed using the femtosecond fluorescence up-conversion technique. *Molecules* **25**, 1–16.
50. Laos, R., C. Lampropoulos and S. A. Benner (2019) The surprising pairing of 2-aminoimidazo[1,2-a][1,3,5]triazin-4-one, a component of an expanded DNA alphabet. *Acta Crystallogr. Sect. C Struct. Chem.* **75**, 22–28.
51. Granovsky, A. A. (2011) Extended multi-configuration quasi-degenerate perturbation theory: The new approach to multi-state multi-reference perturbation theory. *J. Chem. Phys.* **134**, 214113.
52. Shiozaki, T., W. Győrffy, P. Celani and H.-J. Werner (2011) Communication: Extended multi-state complete active space second-order perturbation theory: Energy and nuclear gradients. *J. Chem. Phys.* **135**, 081106.
53. Lakowicz, J. R. (2006) *Principles of fluorescence spectroscopy*. Springer US, Boston, MA. https://doi.org/10.1007/978-0-387-46312-4
54. Chen, R. F. (1967) Fluorescence quantum yields of tryptophan and tyrosine. *Anal. Lett.* **1**, 35–42.
55. Brister, M. M. and C. E. Crespo-Hernández (2019) Excited-state dynamics in the RNA nucleotide uridine 5′-monophosphate investigated using femtosecond broadband transient absorption spectroscopy. *J. Phys. Chem. Lett.* **10**, 2156–2161.
56. Reichardt, C., R. A. Vogt and C. E. Crespo-Hernández (2009) On the origin of ultrafast nonradiative transitions in nitro-polycyclic aromatic hydrocarbons: Excited-state dynamics in 1-nitronaphthalene. *J. Chem. Phys.* **131**, 224518.
57. Pollum, M. and C. E. Crespo-Hernández (2014) Communication: The dark singlet state as a doorway state in the ultrafast and efficient intersystem crossing dynamics in 2-thiothymine and 2-thiouracil. *J. Chem. Phys.* **140**, 071101.
58. Arpa, E. M., M. M. Brister, S. J. Hoehn, C. E. Crespo-Hernández and I. Corral (2020) On the origin of the photostability of DNA and RNA monomers: Excited state relaxation mechanism of the pyrimidine chromophore. *J. Phys. Chem. Lett.* **11**, 5156–5161.
59. Snellenburg, J. J., S. Laptenok, R. Seger, K. M. Mullen and I. H. M. van Stokkum (2012) Glotaran: A Java-based graphical user interface for the R package TIMP. *J. Stat. Softw.* **49**, 1–22.
60. Van Stokkum, I. H. M., D. S. Larsen and R. Van Grondelle (2004) Global and target analysis of time-resolved spectra. *Biochim. Biophys. Acta Bioenerg.* **1657**, 82–104.
61. Giussani, A., J. Segarra-Martí, D. Roca-Sanjuán and M. Merchán (2015) Excitation of nucleobases from a computational perspective I: Reaction paths. In *Photoinduced Phenomena in Nucleic Acids I: Nucleobases in the Gas Phase and in Solvents* (Edited by M. Barbatti, A. C. Borin and S. Ullrich), pp. 57–97. Springer International Publishing, Cham.
62. Dunning, T. H. (1989) Gaussian basis sets for use in correlated molecular calculations. I. The atoms boron through neon and hydrogen. *J. Chem. Phys.* **90**, 1007–1023.
63. Ghigo, G., B. O. Roos and P.-Å. Malmqvist (2004) A modified definition of the zeroth-order Hamiltonian in multiconfigurational perturbation theory (CASPT2). *Chem. Phys. Lett.* **396**, 142–149.
64. Forsberg, N. and P.-Å. Malmqvist (1997) Multiconfiguration perturbation theory with imaginary level shift. *Chem. Phys. Lett.* **274**, 196–204.
65. De Vico, L., M. Olivucci and R. Lindh (2005) New general tools for constrained geometry optimizations. *J. Chem. Theory Comput.* **1**, 1029–1037.
66. Miertuš, S., E. Scrocco and J. Tomasi (1981) Electrostatic interaction of a solute with a continuum. A direct utilizaion of ab initio molecular potentials for the prevision of solvent effects. *Chem. Phys.* **55**, 117–129.
67. Frisch, M. J., G. W. Trucks, H. B. Schlegel, G. E. Scuseria, M. A. Robb, J. R. Cheeseman and E. Al. Gaussian 09 Revision D.01.
68. Fdez. Galván, I., M. Vacher, A. Alavi, C. Angeli, F. Aquilante, J. Autschbach, J. J. Bao, S. I. Bokarev, N. A. Bogdanov, R. K. Carlson, L. F. Chibotaru, J. Creutzberg, N. Dattani, M. G. Delcey, S. S. Dong, A. Dreuw, L. Freitag, L. M. Frutos, L. Gagliardi, F. Gendron, A. Giussani, L. González, G. Grell, M. Guo, C. E. Hoyer, M. Johansson, S. Keller, S. Knecht, G. Kovačević, E. Källman, G. Li Manni, M. Lundberg, Y. Ma, S. Mai, J. P. Malhado, P. Å. Malmqvist, P. Marquetand, S. A. Mewes, J. Norell, M. Olivucci, M. Oppel, Q. M. Phung, K. Pierloot, F. Plasser, M. Reiher, A. M. Sand, I. Schapiro, P. Sharma, C. J. Stein, L. K. Sørensen, D. G. Truhlar, M. Ugandi, L. Ungur, A. Valentini, S. Vancoillie, V. Veryazov, O. Weser, T. A. Wesołowski, P. O. Widmark, S. Wouters, A. Zech, J. P. Zobel and R. Lindh (2019) OpenMolcas: From source code to insight. *J. Chem. Theory Comput.* **15**, 5925–5964.
69. Aquilante, F., J. Autschbach, A. Baiardi, S. Battaglia, V. A. Borin, L. F. Chibotaru, I. Conti, L. De Vico, M. Delcey, I. Fdez Galván, N. Ferré, L. Freitag, M. Garavelli, X. Gong, S. Knecht, E. D. Larsson, R. Lindh, M. Lundberg, P. Å. Malmqvist, A. Nenov, J. Norell, M. Odelius, M. Olivucci, T. B. Pedersen, L. Pedraza-González, Q. M.

Phung, K. Pierloot, M. Reiher, I. Schapiro, J. Segarra-Martí, F. Segatta, L. Seijo, S. Sen, D. C. Sergentu, C. J. Stein, L. Ungur, M. Vacher, A. Valentini and V. Veryazov (2020) Modern quantum chemistry with [open]Molcas. *J. Chem. Phys.* **152**, 214117.

70. Valverde, D., A. V. Sanches de Araujo, A. Carlos Borin and S. Canuto (2017) Electronic structure and absorption spectra of fluorescent nucleoside analogues. *Phys. Chem. Chem. Phys.* **19**, 29354–29363.
71. Georg, H. C. and S. Canuto (2012) Electronic properties of water in liquid environment. A sequential QM/MM study using the free energy gradient method. *J. Phys. Chem. B* **116**, 11247–11254.
72. Bistafa, C., H. C. Georg and S. Canuto (2014) Combining ab initio multiconfigurational and free energy gradient methods to study the π–π* excited state structure and properties of uracil in water. *Comput. Theor. Chem.* **1040–1041**, 312–320.
73. Coutinho, K., H. C. Georg, T. L. Fonseca, V. Ludwig and S. Canuto (2007) An efficient statistically converged average configuration for solvent effects. *Chem. Phys. Lett.* **437**, 148–152.
74. Georg, H. C., K. Coutinho and S. Canuto (2007) Solvent effects on the UV-visible absorption spectrum of benzophenone in water: A combined Monte Carlo quantum mechanics study including solute polarization. *J. Chem. Phys.* **126**, 034507.
75. Eberlein, L., F. R. Beierlein, N. J. R. Van Eikema Hommes, A. Radadiya, J. Heil, S. A. Benner, T. Clark, S. M. Kast and N. G. J. Richards (2020) Tautomeric equilibria of nucleobases in the Hachimoji expanded genetic alphabet. *J. Chem. Theory Comput.* **16**, 2766–2777.
76. Woon, D. E. and T. H. Dunning (1995) Gaussian basis sets for use in correlated molecular calculations. V. Core-valence basis sets for boron through neon. *J. Chem. Phys.* **103**, 4572–4585.
77. Orozco-Gonzalez, Y., M. Manathunga, M. D. C. Marín, D. Agathangelou, K. H. Jung, F. Melaccio, N. Ferré, S. Haacke, K. Coutinho, S. Canuto and M. Olivucci (2017) An average solvent electrostatic configuration protocol for QM/MM free energy optimization: Implementation and application to rhodopsin systems. *J. Chem. Theory Comput.* **13**, 6391–6404.
78. Leonard, P., D. Kondhare, X. Jentgens, C. Daniliuc and F. Seela (2019) Nucleobase-functionalized 5-Aza-7-deazaguanine Ribo- and 2′-deoxyribonucleosides: Glycosylation, pd-assisted cross-coupling, and photophysical properties. *J. Org. Chem.* **84**, 13313–13328.
79. Kasha, M. (1950) Characterization of electronic transitions in complex molecules. *Discuss. Faraday Soc.* **9**, 14–19.
80. Karunakaran, V., K. Kleinermanns, R. Improta and S. A. Kovalenko (2009) Photoinduced dynamics of guanosine monophosphate in water from broad-band transient absorption spectroscopy and quantum-chemical calculations. *J. Am. Chem. Soc.* **131**, 5839–5850.
81. Ma, C., C. C.-W. Cheng, C. T.-L. Chan, R. C.-T. Chan and W.-M. Kwok (2015) Remarkable effects of solvent and substitution on the photo-dynamics of cytosine: A femtosecond broadband time-resolved fluorescence and transient absorption study. *Phys. Chem. Chem. Phys.* **17**, 19045–19057.
82. Lee, J., J. R. Challa and D. W. McCamant (2017) Ultraviolet light makes dGMP floppy: Femtosecond stimulated Raman spectroscopy of 2′-Deoxyguanosine 5′-monophosphate. *J. Phys. Chem. B* **121**, 4722–4732.
83. Onidas, D., D. Markovitsi, S. Marguet, A. Sharonov and T. Gustavsson (2002) Fluorescence properties of DNA nucleosides and nucleotides: A refined steady-state and femtosecond investigation. *J. Phys. Chem. B* **106**, 11367–11374.